European Polymer Journal 200 (2023) 112551

Contents lists available at ScienceDirect

European Polymer Journal

journal homepage: www.elsevier.com/locate/europolj

Construction of three-dimensional porous organic polymers with enhanced CO_2 uptake performance *via* solid-state thermal conversion from tetrahedral benzoxazine-linked precursor

Mohamed Gamal Mohamed [a,b,*], Chia-Chi Chen [a], Kan Zhang [c], Shiao-Wei Kuo [a,d,*]

[a] Department of Materials and Optoelectronic Science, Center for Functional Polymers and Supramolecular Materials, National Sun Yat-Sen University, Kaohsiung 804, Taiwan
[b] Department of Chemistry, Faculty of Science, Assiut University, Assiut 71515, Egypt
[c] Research School of Polymeric Materials, School of Materials Science and Engineering, Jiangsu University, Zhenjiang 212013, China
[d] Department of Medicinal and Applied Chemistry, Kaohsiung Medical University, Kaohsiung 807, Taiwan

ARTICLE INFO

Keywords:
Tetraphenylmethane
Benzoxazine
Polybenzoxazine
Thermal ring-opening polymerization
Porous organic polymers
CO_2 uptake

ABSTRACT

Porous organic polymers (POPs) with three-dimensional (3D) linkages have drawn great interest due to their potential applications in separation, adsorption, and sensing fields. Herein, a new 3D benzoxazine (BZ)-linked porous organic polymer (TPM-BZ-Py POP) was synthesized by linking a tetrahedral benzoxazine (TPM-BZ-Br_4) with tetraethynylpyrene (Py-T) *via* Sonogashira coupling. Specifically, the synthesis of the tetrahedral benzoxazines with four oxazine rings in a single monomer involved the utilization of Schiff base formation, $NaBH_4$ reduction as well as Mannich condensation reactions. To confirm the chemical structure of the benzoxazine monomers and their corresponding polybenzoxazines, Fourier transform infrared (FTIR), proton nuclear magnetic resonance (^{1}H NMR), and carbon nuclear magnetic resonance (^{13}C NMR) spectroscopy techniques were employed. The pore volume and specific surface area of the 3D TPM-BZ-Py POP were determined through N_2 adsorption/desorption isotherms, and they were found to be 0.52 cm^3/g and 185 m^2/g, respectively. In addition, the solid-state chemical transformation occurred during thermal ring-opening polymerization (ROP), and the resulting 3D poly(TPM-BZ-Py) POP displayed higher CO_2 capture ability (1.81 mmol/g) compared with TPM-BZ-Py POP (0.60 mmol/g) at room temperature. Such enhancement observed in poly(TPM-BZ-Py) POP was proposed to be caused by the formation of phenolic units and Mannich bridges within the polymer network by taking into consideration the structural transformation during the ring-opening polymerization (ROP). The functionalities in poly(TPM-BZ-Py) have great potential to interact with CO_2 molecules through strong intermolecular hydrogen bonding or acid/base interactions, which further supports the benefit of incorporating oxazine rings into POP frameworks.

1. Introduction

Porous organic polymers (POPs) possessing pores and large specific surface areas, such as conjugated microporous polymers (CMPs) and covalent organic frameworks (COFs), have been extensively explored for a wide range of applications. These include gas capture/separation, hydrogen evolution, energy storage, chemical sensing, and photocatalysis [1–12]. In the synthesis of POPs, various organic reactions, including Schiff base, Yamamoto, Sonogashira, Suzuki, and Friedel couplings, have been widely employed to introduce different covalent bonds such as imine, hydrazine, imide, triazine, and boroxine units [13–22]. For example, our group has developed various CMPs using building blocks such as pyrene (Py), tetraphenylethylene (TPE), and triphenylamine (TPA) through Schiff base, Suzuki and Sonogashira–Hagihara cross-couplings [23–38]. These CMPs have displayed promising performance in applications such as H_2 production, energy storage, and CO_2 capture, and these diverse synthesized strategies and the combination of various building blocks allow us to tailor the thermal and optoelectronic properties of the resulting POPs for potential applications [23–38].

* Corresponding authors at: Department of Materials and Optoelectronic Science, Center for Functional Polymers and Supramolecular Materials, National Sun Yat-Sen University, Kaohsiung 804, Taiwan.
E-mail addresses: magamal.eldin12@yahoo.com (M. Gamal Mohamed), kuosw@faculty.nsysu.edu.tw (S.-W. Kuo).

https://doi.org/10.1016/j.eurpolymj.2023.112551
Received 27 July 2023; Received in revised form 22 September 2023; Accepted 28 October 2023
Available online 30 October 2023

The incorporation of special chemical functionalities into the frameworks of POPs could significantly affect their surface properties and surface areas for their further applications. For instance, imine-linked POPs have been shown to convert transformation into the quinolone, oxazole, amine/amide, and thiazole functional groups [39–44]. In addition, Yaghi et al. also proposed that the imine-COF could transfer into the thiocarbamate and carbamate-linked COFs featuring higher surface area through multistep solid-state chemical transformation procedures [45]. Furthermore, Ma et al. have utilized the imine-COF to achieve the high surface area of benzoxazine-linked COF (>650 m^2/g) through reduction and Mannich reactions with benzyl aldehyde or CH_2O [46].

Benzoxazines represent a new type of thermosetting material that could form inter- and intramolecular hydrogen bonding after thermal curing of oxazine units without adding any curing agent or catalyst, which are widely used for low-dielectric materials, aerospace, and coatings [47–65]. In general, benzoxazine monomers can be prepared by using aromatic phenols, primary amines, and CH_2O through the Mannich reaction, and the synthesis of benzoxazine-linked POPs has also been proposed featuring high surface areas recently [29,31,36]. These advantages of functionality incorporation and surface area modulation are able to contribute to expanding the possibility for tailored applications. For example, we designed a nitrile-functionalized benzoxazine from 1,3,5-tris(4-aminophenoxy)benzene and 4-cyanophenol with CH_2O, which exhibited the high surface areas to form triazine frameworks during cyclotrimerization [64]. On the other hand, we also proposed a benzoxazine-linked POP that displayed a relatively lower surface area (ca. 72 m^2/g) [65]. In another study, Tan et al. used one-step Mannich reaction to synthesize three different types of benzoxazine-linked POPs from triphenol, and CH_2O with three different amines with surface areas exceeding 230 m^2/g [66]. We further expanded the scope of benzoxazine-linked POPs by synthesizing various derivatives featuring a high surface area (>320 m^2/g) through Sonogashira–Hagihara coupling from different kinds of brominated benzoxazine derivatives with various ethynyl functionalized building blocks. However, these previously reported investigations were all two-dimensional (2D) benzoxazine-linked POPs, where the flat sheets were typically stacked into the face-to-face model, resulting in strong π-π interactions. In contrast, 3D POPs offer numerous open sites and pore confinement effects, which could lead to enhanced catalysis and adsorption efficiency. For example, Sun et al. synthesized two different benzoxazine-linked POPs through brominated mono-benzoxazine derivatives by using Sonogashira–Hagihara coupling with tetrahedral silicone-core building bock, which reached a high surface area exceeding 630 m^2/g [67]. However, so far achieving 3D POPs starting from tetrahedral benzoxazine has never been investigated.

In order to synthesize 3D BZ-linked POPs, we proposed using a tetrahedral building block, tetra(*p*-aminophenyl)methane (TPM) [68,69], which contains four amine units as the starting monomer. The synthesis of the target brominated tetrahedral benzoxazine derivative, TPM-BZ-Br_4 monomer, involved three steps including Schiff base reaction from TPM with 4-bromosalicylaldehyde, reduction with $NaBH_4$ and Mannich condensation with CH_2O. Finally, 3D BZ-linked POPs were successfully achieved through Sonogashira coupling from TPM-BZ-Br_4 with Py-T building blocks to provide 3D TPM-BZ-Py POP by using Pd$(PPh_3)_4$ as a catalyst and DMF/Et_3N as a co-solvent for 3 days at 90 °C under a N_2 atmosphere. The newly obtained 3D TPM-BZ-Py POP could possess the solid-state chemical transformation during thermal ROP to form phenolic OH units and Mannich bridges, which improve the CO_2 capture ability. To the best of our knowledge, the current study provides the first example of 3D benzoxazine-linked POP based on tetrahedral benzoxazine. The rational design and synthesis of this type of 3D POP with specific functionalities explore a new way to promote the development of POPs.

2. Experiment section

2.1. Materials

Salicylaldehyde (98 %), tetraphenylmethane (TPM, 97 %), acetic anhydride (Ac_2O), acetic acid (AcOH), 4-bromosalicylaldehyde (97 %), sodium borohydride ($NaBH_4$, 99 %), DMF, EtOH, DMAc, MeOH, triethylamine (Et_3N), tetrahydrofuran (THF), copper iodide (CuI, 98 %), triphenylphosphine (PPh_3, 99 %) and Pd$(PPh_3)_4$ (99.99 %) were bought them from Sigma-Aldrich. The synthesis of 1,3,6,8-tetraethynylpyrene (Py-T) followed our previous method (Scheme S1) [70].

2.2. Tetra(p-aminophenyl)methane [TPM-4NH_2]

To initiate the reaction, 3 g of TPM (9.36 mmole) were vigorously stirred with 16.22 mL of fuming nitric acid at a temperature of 40 °C. Following that, a mixture of 5.1 mL of Ac_2O and 10.14 mL of AcOH was slowly added while continuing the agitation for 1 h. The resulting product was a yellow solid, which was separated through filtration. The yellow solid was further purified by recrystallization using THF, resulting in the formation of yellow crystals (TPM-4NO_2). A solution of TPM-4NO_2 (2 g, 4 mmole) in 50 mL of THF was prepared. 10 wt% of Pd/C was introduced into the solution. The resulting mixture was subjected to purging with N_2 and H_2 gases. Following three days of stirring under H_2 gas pressure at room temperature, the reaction mixture was filtered using celite to separate the Pd/C powder. After the Pd/C powder was removed, TPM-4NH_2 was obtained as a white powder from the filtrate (Scheme S2).

2.3. TPM-SB

TPM-4NH_2 (0.8 g, 2.1 mmol), salicylaldehyde (0.879 mL, 10.5 mmol), and absolute EtOH (75 mL) were added to a 150 mL round flask. The solution combination was refluxed for 24 h at a temperature of 75 to 80 °C. It was filtered, then washed three times with EtOH before being dried to produce a yellow solid. Yield: 91 %. FTIR: 3300 (OH), 3060 (C═C—H), 1570. ^{1}H NMR (DMSO-d_6, 500 MHz, δ, ppm): 13.0 (OH), 8.98 (N═C—H), 7.63–7.22 (C—H aromatic protons). ^{13}C NMR (DMSO-d_6, 125 MHz, δ, ppm): δ = 161.14 (N═C—H), 146.8–117.2 (aromatic carbons), 63.9 (quaternary carbon atom). High-resolution ES-MS (*m/z*): calcd for ($C_{53}H_{40}N_4O_4$), 796.93; found, 797.20 (Figure S1).

2.4. TPM-R

TPM-SB (1.50 g, 1.88 mmol), $NaBH_4$ (0.854 g, 22.6 mmol), and DMAc (10 mL) were added to the round flask (100 mL). The solution mixture was stirred and kept at 25 °C for 24 h. The solution mixture was put into a large amount of water (1 L) and then filtered, and a yellow solid was obtained after washing 3 with water. Yield: 79 %. FTIR: 3410 (NH), 3300 (OH unit). ^{1}H NMR (DMSO-d_6, 500 MHz, δ, ppm): δ = 8.30 (OH), 5.74 (NH), 7.20–6.42 (aromatic protons), 4.1 ($HNCH_2$). ^{13}C NMR (DMSO-d_6, 125 MHz, δ, ppm): δ = 156.05–111.50 (aromatic carbons), 61.5 (quaternary carbon atom), 41.9 ($HNCH_2$). High-resolution ES-MS (*m/z*): calcd for ($C_{53}H_{48}N_4O_4$), 804.99; found, 805.30 (Figure S2).

2.5. TPM-BZ

Added a mixture of TPM-R (1 g, 1.24 mmol), CH_2O (0.17 g, 5.6 mmol), 1,4-dioxane (DO, 80 mL) and EtOH (40 mL) to round flask (250 mL). The solution mixture was heated at 90 °C for 1 day. A rotary evaporator was used to eliminate the solvent., added MeOH to filter, and washed 3 times with MeOH. Then, a white solid was obtained. Yield: 97 %. FTIR: 1230, 944. ^{1}H NMR (DMSO-d_6, 500 MHz): 7.06–6.70, 5.36 (OCH_2N), 4.57 ($ArCH_2N$). ^{13}C NMR (DMSO-d_6, 125 MHz, δ, ppm): 154.8–116.7 (aromatic carbons), 78.7 (OCH_2N), 61.8 (Quaternary carbon atom), 48.8 ($ArCH_2N$). High-resolution ES-MS (*m/z*): calcd for

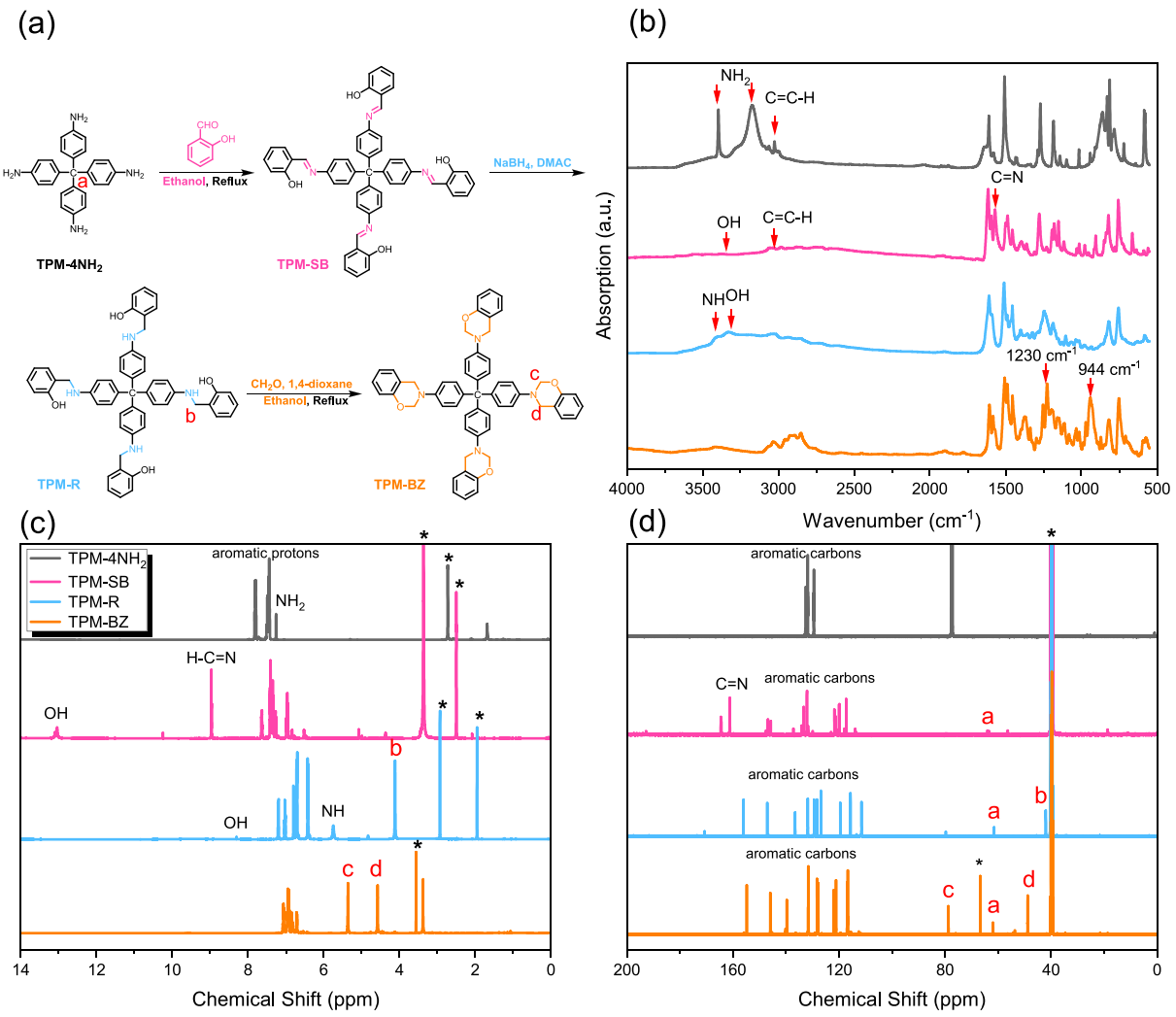

Fig. 1. (a) Synthesis of TPM-BZ from TPM-4NH_2, TPM-SB and TPM-R, and each corresponding (b) FTIR, (c) ^{1}H NMR (*= DMSO-d_6, and (d) ^{13}C NMR spectra (*= 1,4-dioxane and DMSO-d_6).

($C_{57}H_{48}N_4O_4$), 853.04; found, 853.3 (Figure S3).

2.6. TPM-SB-Br_4

TPM-4NH_2 (1.00 g, 2.63 mmol), 4-bromosalicylaldehyde (2.11 g, 10.5 mmol), and absolute EtOH (80 mL) were added to the round flask. The solution mixture was heated at 75 °C and refluxed for 24 h. The solution mixture was filtered, then washed with absolute EtOH three times and dried to obtain a yellow solid. Yield: 73 %. FTIR: 3340 (OH unit), 3030, 1560 (C═N), 611(C-Br). ^{1}H NMR (DMSO-d_6, 500 MHz, δ, ppm): 13.4 (OH group), 8.96 (N═C—H), 7.57–7.19. ^{13}C NMR (DMSO-d_6, 125 MHz, δ, ppm): 161.9 (N═C—H), 146.0–119.2 (aromatic carbons), 63.4 (quaternary carbon atom). High-resolution ES-MS (m/z): calcd for ($C_{53}H_{36}Br_4N_4O_4$), 1112.51; found, 1190.7 (Figure S4).

2.7. TPM-R-Br_4

TPM-SB-Br_4 (1.80 g, 1.6 mmol), $NaBH_4$ (0.79 g, 2.0 mmol), and DMAc (20 mL) were added to the round flask. Under the N_2 atmosphere, the solution mixture was agitated and held at 25 °C for one day. After one day, the solution mixture was put into a large amount of water (1L) and then filtered, and a yellow solid was obtained after washing with H_2O. Yield: 52 %. FTIR: 3400 (NH), 3310. ^{1}H NMR (DMSO-d_6, 500 MHz, δ, ppm): 7.93 (OH), 5.79 (NH), 7.06–6.71 (aromatic protons), 4.07 ($HNCH_2$). ^{13}C NMR (DMSO-d_6, 125 MHz, δ, ppm): 157.9–111.5 (aromatic carbons), 61.37 (quaternary carbon atom), 41.9 ($HNCH_2$). HR ES-MS (m/z): calcd for ($C_{53}H_{44}Br_4N_4O_4$), 1120.58; found, 1120.9 (Figure S5).

2.8. TPM-BZ-Br_4

TPM-R-Br_4 (0.85 g, 0.76 mmol), CH_2O (0.10 g, 3.3 mmol), 1,4-dioxane (DO, 80 mL) and EtOH (40 mL) were added to a round flask (250 mL) and stirred together for 1 day at 90–100 °C. A rotary evaporator was used to eliminate the solvent, added MeOH to filter, and washed 3 times with MeOH. Then, a white solid was obtained. Yield: 81.8 %. FTIR: 1230, 944. ^{1}H NMR (500 MHz, δ, ppm): 7.01–6.91, 5.39 (OCH_2N), 4.55 ($ArCH_2N$). ^{13}C NMR (DMSO-d_6, 125 M Hz, δ, ppm): 155.8–116.9 (aromatic carbons), 79.1 (OCH_2N), 61.89 (quaternary carbon atom), 48.4 ($ArCH_2N$). HR ES-MS (m/z): calcd for ($C_{57}H_{44}Br_4N_4O_4$), 1168.62; found, 1168.80 (Figure S6).

2.9. Three-dimensional (3D) TPM-BZ-Py POP

A solution of TPM-BZ-Br_4 (200 mg), Py-T (40 mg), CuI (7 mg), PPh_3 (7 mg,), $Pd(PPh_3)_4$ (50 mg), DMF (7 mL), and Et_3N (7 mL) were added to round flask (25 mL) and stirred together for 3 days at 90 °C under N_2 atmosphere. After filtration, it was washed with MeOH, Acetone, and THF, then dried to obtain a white powder of TPM-BZ-Py POP. Yield: 60 %.

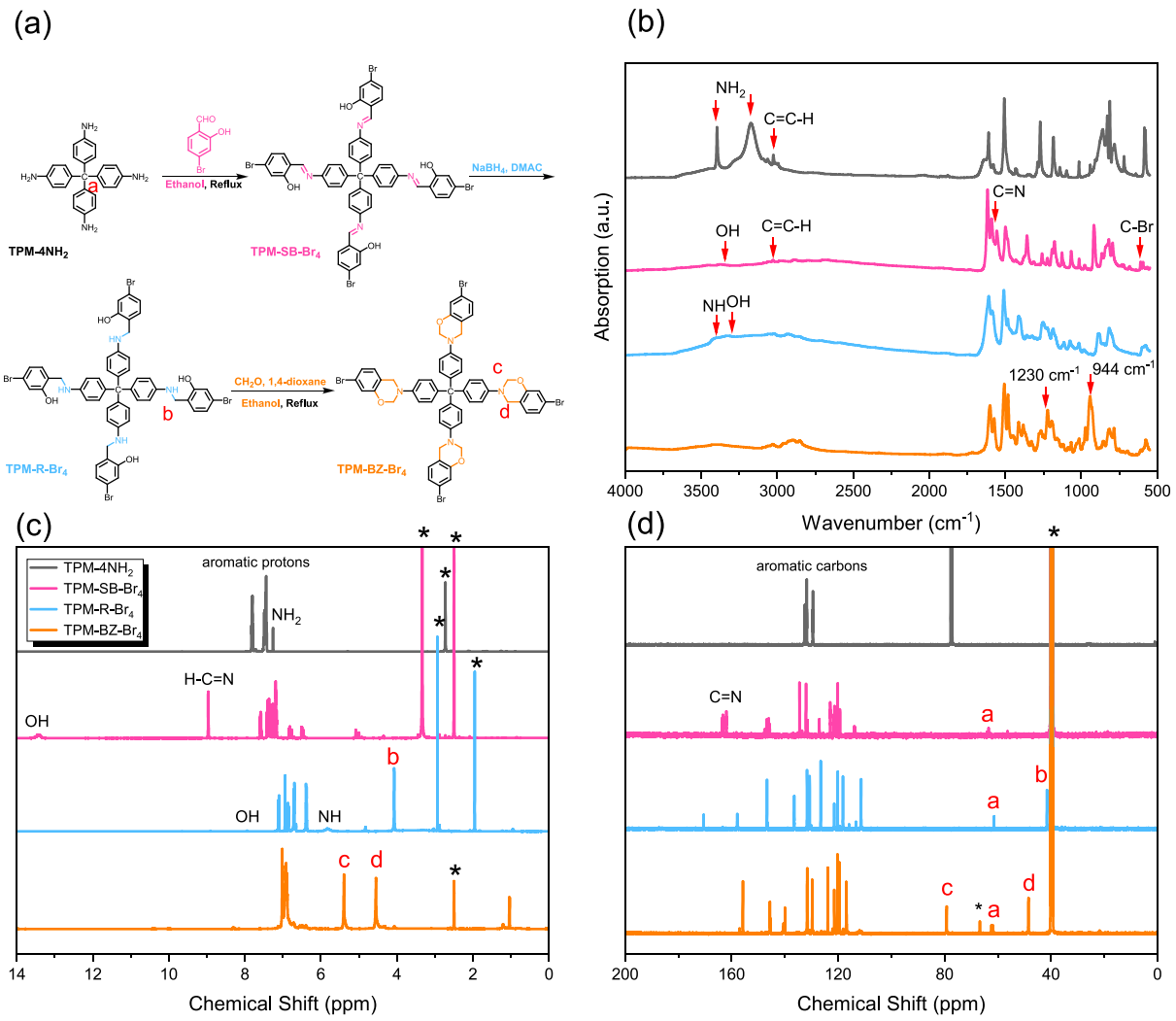

Fig. 2. (a) Synthesis of TPM-BZ-Br_4 from TPM-4NH_2, TPM-SB-Br_4 and TPM-R-Br_4, and each corresponding (b) FTIR, (c) ^{1}H NMR (DMSO-d_6), and (d) ^{13}C NMR spectra (*= 1,4-dioxane and DMSO-d_6).

2.10. Thermal polymerization of TPM-BZ, TPM-BZ-Br$_4$ Monomers, and TPM-BZ-Py POP

TPM-BZ, TPM-BZ-Br4, and TPM-BZ-Py POP underwent thermal polymerization at the following temperatures for 2 h each: 100, 150, 180, 210, and 270 °C to obtain poly(TPM-BZ), poly(TPM-BZ-Br4) and poly(TPM-BZ-Py) POP.

3. Results and discussion

3.1. Synthesis of the TPM-BZ monomer

Fig. 1(a) presents the reaction steps for TPM-BZ, which is designed as the model compound from TPM-4NH_2, and its corresponding synthesis involves three main steps. Firstly, TPM-4NH_2 was reacted with salicylaldehyde to obtain TPM-SB through a Schiff base reaction. Secondly, TPM-R was obtained through the $NaBH_4$-mediated reduction step, which converted the imine functionality in TPM-SB to the TPM-B. Finally, the Mannich condensation was performed with CH_2O in 1,4 dioxane/EtOH at 90 °C for 1 day to yield the TPM-BZ monomer under the protection of an N_2 atmosphere. Fig. 1(b) shows the FTIR spectra of the TPM-4NH_2 monomer featuring the absorption peaks for NH_2 and C═C—H units at 3400, 3170, and 3030 cm^{-1}, respectively. Besides, the FTIR spectrum of fTPM-SB displays the absorption peaks for OH, C═C—H, and C═N units at 3300, 3060, and 1570 cm^{-1}, respectively; however, the signals for the NH_2 unit at 3400 and 3170 cm^{-1} were disappeared after Schiff base reaction. After reduction to form TPM-R, the band of C═N unit at 1570 cm^{-1} was disappeared, leaving only NH (3410 cm^{-1}) and OH (3300 cm^{-1}) absorptions. The new absorption bands, which represent the C-O-C and oxazine rings, were finally seen at 1230 and 944 cm^{-1} following Mannich condensation to create TPM-BZ. The observed changes and shifts in FTIR analyses provide evidence of the formation of TPM-BZ. The ^{1}H NMR spectra as shown in Fig. 1(c) of the TPM-4NH_2 monomer contain featured signals for aromatic protons and NH_2 at 7.81–7.44 and 7.26 ppm, respectively. Upon the Schiff base was formed, the signal corresponding to the NH_2 unit in TPM-SB was disappeared, while new signals were appeared at 13.0, 8.98, and 7.63–7.22 ppm, representing phenolic OH, N═C–H, and aromatic protons, respectively. After the reduction reaction of TPM-SB and the formation of TPM-R, the signal for N═C—H units at 8.98 ppm was vanished, featuring peaks for the OH, NH, and aromatic protons at 8.30, 5.74, and 7.20–6.42 ppm, respectively, and a new signal was also observed at 4.1 ppm for the HNC**H**$_2$ unit. Finally, after the Mannich condensation, the ^{1}H NMR spectrum of the TPM-BZ monomer had peaks at 7.06–6.70, 5.36, and 4.57 ppm, due to aromatic protons, OCH_2N, and $ArCH_2N$, respectively. The ratio of the signals of 5.36 ppm (*c*, OCH_2N) and 4.57 ppm (*d*, $ArCH_2N$) to the protons of the oxazine ring is 1:1, while the signal of the $HNCH_2$ unit disappears completely in the TPM-BZ

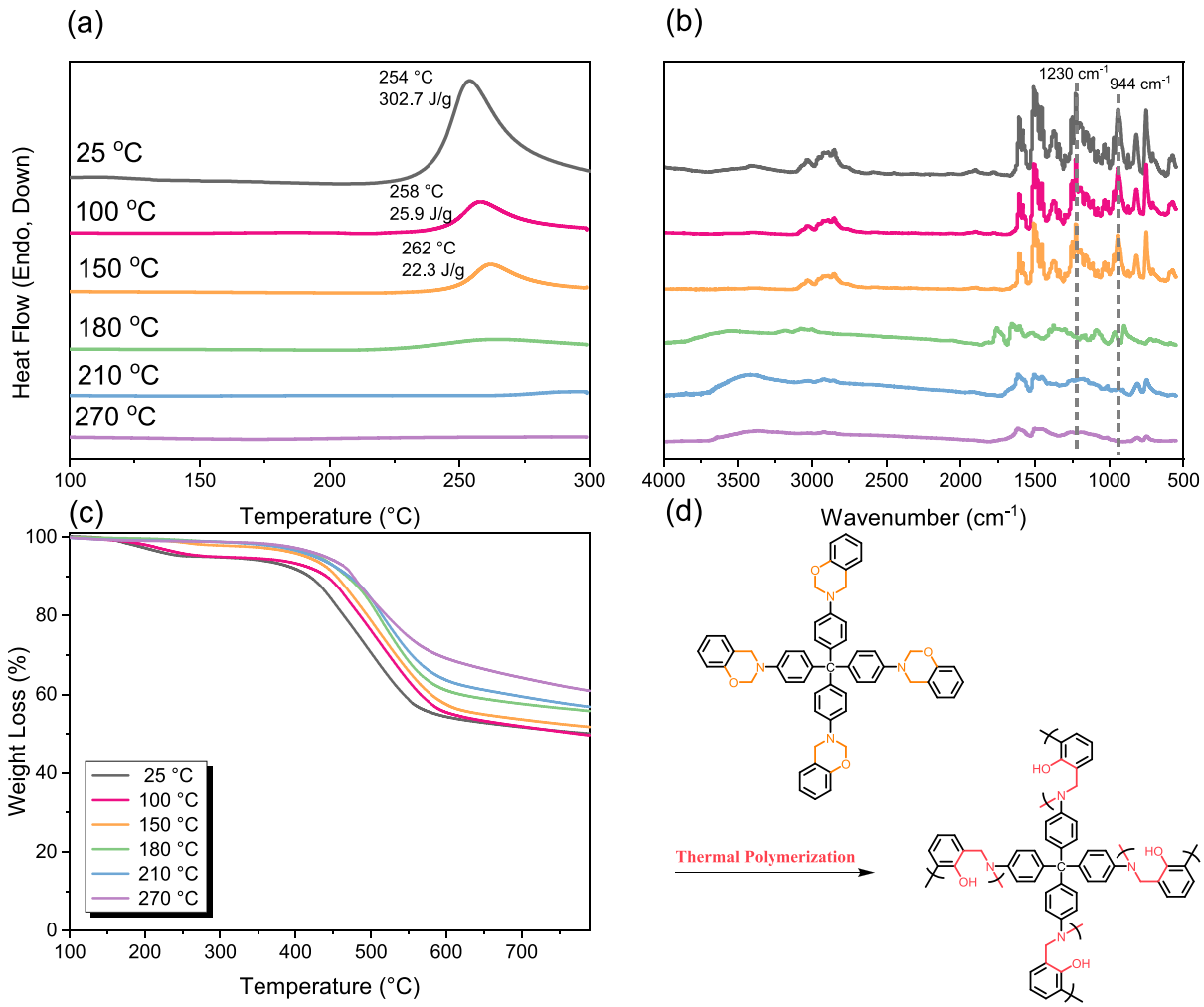

Fig. 3. Following thermal polymerization at various temperatures, the TPM-BZ monomer underwent (a) DSC, (b) FTIR spectra, and (c) TGA. (d) A schematic illustration of the TPM-BZ monomer's chemical structure following thermal ROP.

monomer. In addition, the ^{13}C NMR spectrum (Fig. 1d) of the TPM-SB contains signals at 161.1, 146.8–117.2, and 63.9 ppm, representing the N═C—H, aromatic carbons, and quaternary carbon atom, respectively. After reduction and TPM-R synthesis, the signal from the N═CH group at 161.14 ppm vanished, and a new peak for the $HNCH_2$ unit appeared at 41.9 ppm. Finally, TPM-BZ showed the signals at 54.8–116.7 (aromatic carbons), 78.7 (OCH_2N), 61.8 (quaternary carbon atom), and 48.8 ppm ($ArCH_2N$) after Mannich condensation, while the signal for the $HNCH_2$ units was disappeared at 41.9 ppm in TPB-BZ monomer. We have confirmed the successful synthesis of TPM-BZ monomer through FTIR and NMR analysis, and its purity has been further supported by a high-resolution mass spectrum and experimental molecular weight determination (Figure S3).

3.2. Synthesis of the TPM-BZ-Br_4 monomer

In order to obtain 3D POP with benzoxazine linkage, a novel brominated tetrahedral benzoxazine (TPM-BZ-Br_4) was designed and synthesized. Fig. 2(a) displays the synthetic procedures of the TPM-BZ-Br_4 monomer, which are identical to those of the TPM-BZ monomer and also involve three main steps. Initially, we reacted TPM-$4NH_2$ with 4-bromosalicylaldehyde to provide TPM-SB-Br_4 through a Schiff base formation. Subsequently, the $NaBH_4$-mediated reduction was employed to obtain TPM-R-Br_4. At last, the TPM-BZ-Br_4 monomer was produced by Mannich condensation with CH_2O in 1,4 dioxane/EtOH mixture at 90–100 °C for 1 day. The FTIR spectra displayed in Fig. 2(b) of TPM-SB-Br_4 show the absorption signals at 3340, 3030, 1560, and 611 cm^{-1}, representing the OH, C═C—H, C═N, and C—Br functional groups, respectively and the signals for the NH_2 group at 3400 and 3170 cm^{-1} was absent of TPM-$4NH_2$ resulting from Schiff base formation. Upon reduction to form TPM-R-Br_4, the single for the C═N unit at 1560 cm^{-1} was vanished, leaving only the NH (3400 cm^{-1}) and OH (3310 cm^{-1}) absorptions. In addition, new absorption signals for the C-O-C and oxazine rings were observed at 1230 and 944 cm^{-1} after Mannich condensation to form TPM-BZ-Br_4.

The ^1H NMR pattern of the TPM-SB-Br_4 monomer is shown in Fig. 2 (c). After the Schiff base formed in the TPM-$4NH_2$, the signal for the NH_2 unit at 7.26 ppm vanished; however, new signals emerged at different chemical shifts including at 13.4, 8.96, and 7.57–7.19 ppm, representing the OH, N═C—H, and aromatic protons, respectively. Upon reduction to form TPM-R-Br_4, the signal corresponding to N═C—H at 8.96 ppm was longer present, with the new featured signals for the OH, NH, and aromatic protons at 7.93, 5.79, and 7.06–6.71 ppm, respectively. Additionally, a new signal

appeared at 4.07 ppm, which corresponds to the $HNCH_2$ unit. Following the Mannich condensation, the profile of the TPM-BZ-Br_4 monomer displayed proton's peaks at 7.01–6.91, 5.39, and 4.55 ppm, representing the aromatic protons, OCH_2N, and $ArCH_2N$, respectively. Notably, the signals at 5.39 ppm (c, OCH_2N) and 4.55 ppm (d, $ArCH_2N$) appeared in a 1:1 ratio, reflecting the presence of the oxazine ring protons. Additionally, the peak corresponding to the $HNCH_2$ unit completely vanished in the ^1H spectrum. The ^{13}C NMR spectrum (Fig. 2

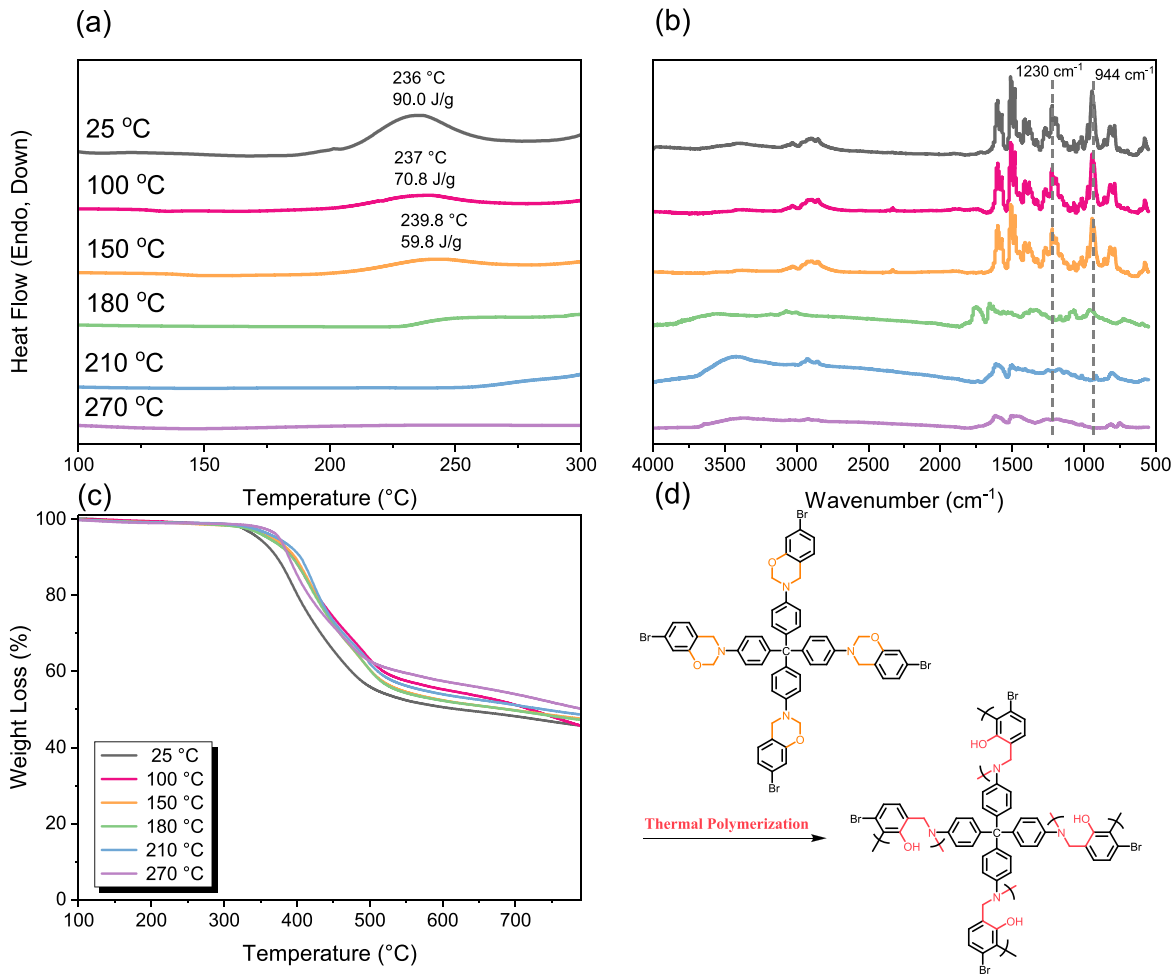

Fig. 4. Following thermal polymerization at various temperatures, the TPM-BZ-Br_4 monomer underwent (a) DSC, (b) FTIR spectra, and (c) TGA. (d) A schematic illustration of the TPM-BZ-Br_4 monomer's chemical structure following thermal ROP.

(d)) of the TPM-SB-Br_4 featured the signals at 161.9, 146.0–119.2, and 63.4 ppm, representing the N═C—H, aromatic carbons, and quaternary carbon atom, respectively. Upon reduction to form the TPM-R-Br_4, the signal corresponding to N═C—H at 161.9 ppm was disappeared in the ^{13}C NMR spectrum. Instead, a new signal emerged at 41.9 ppm for the $HNCH_2$ unit. Finally, following the Mannich condensation, the ^{13}C NMR spectrum of the TPM-BZ-Br_4 featured signals for aromatic carbons, OCH_2N, quaternary carbon atom, and $ArCH_2N$ at 155.8–116.9, 79.1, 61.89, and 48.4 ppm, respectively. Also, no signal was observed at 41.9 ppm, indicating the absence of the $HNCH_2$ unit from the TPM-R-Br_4 monomer. The successful synthesis of the TPM-BZ-Br_4 monomer has also been confirmed by FTIR and NMR analysis. Moreover, the purity of the synthesized compound of TPM-BZ-Br_4 is supported by a high-resolution mass spectrum and experimental molecular weight determination (Figure S6).

3.3. *Thermal polymerization behavior of TPM-BZ and TPM-BZ-Br_4 monomer*

The thermal curing polymerization behavior of TPM-BZ and TPM-BZ-Br_4 monomer was investigated by using DSC, FTIR, and TGA analyses, which were conducted over a range of thermal polymerization temperatures from 25 °C to 270 °C. Fig. 3a shows the DSC analysis of TPM-BZ, which revealed a signal of thermal polymerization exotherm at 254 °C with an enthalpy of 302.7 J g^{-1}. As the thermal curing temperature increases, a signal of thermal polymerization exotherm was decreased. At 270 °C for 2 h, the exothermic peak disappeared completely, meaning the completion of thermal ring-opening polymerization (ROP). This result was further confirmed by FTIR analyses (Fig. 3 (b)), where we focused on specific two bands of the oxazine ring at 944 and 1230 cm^{-1}. The intensity of both signals declined from 25 °C to 210 °C as the thermal polymerization temperature rose. The signal for the oxazine ring totally vanished after 2 h of heat polymerization at 270 °C, confirming the completion of the oxazine ring's ROP, which is consistent with the DSC results. In addition, the TGA analysis (Fig. 3c) displays the thermal stability of the TPM-BZ monomer at various polymerization temperatures.

Fig. 3(d) illustrates the formation of a highly cross-linked 3D network structure of poly(TPM-BZ) as indicated by the increase in char yield and temperature at 10 % weight loss (T_{d10}). The uncured TPM-BZ monomer exhibited a char yield of 50 wt% and T_{d10} at 418 °C. However, after thermal polymerization at 270 °C for 2 h, the T_{d10} value rose to 465 °C with a corresponding char yield of 61 wt%, suggesting the development of a significantly stronger cross-linked network structure.

To further investigate the thermal polymerization behavior of the TPM-BZ-Br_4 monomer, comprehensive studies were conducted utilizing DSC, FTIR, and TGA techniques. The DSC thermal analyses (Fig. 4a) of the uncured TPM-BZ-Br_4 monomer exhibited an exothermic peak at 236 °C with an enthalpy of 90.0 J g^{-1}. Similar to the TPM-BZ monomer, it can be observed that as the curing temperature increased, the enthalpy of the exothermic curing peak gradually decreased, and when the temperature reached 270 °C for 2 h, complete ROP resulted in the disappearance of the curing peak. However, we could observe that the enthalpy of TPM-BZ-Br_4 was lower than that of TPM-BZ because the

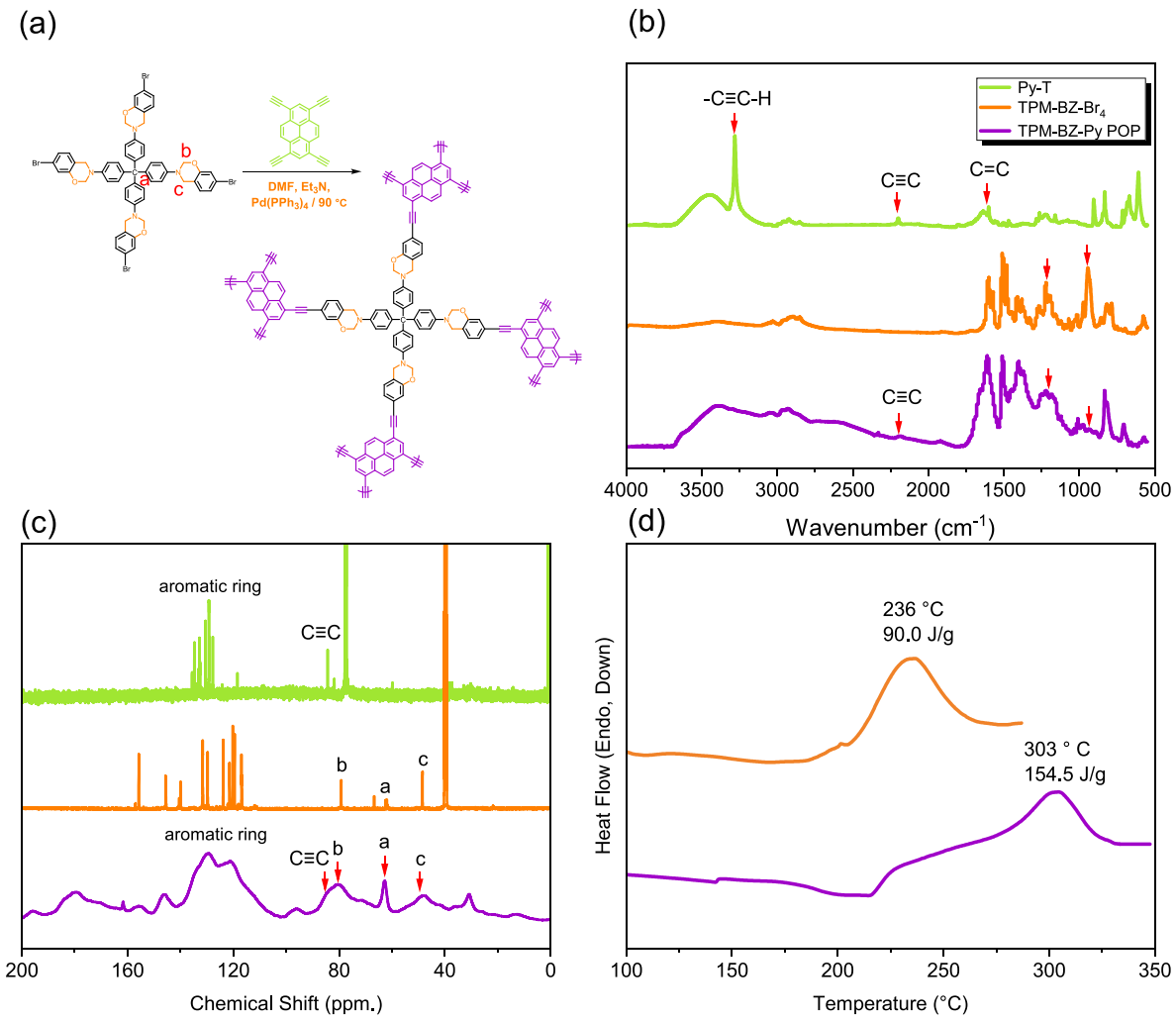

Fig. 5. (a) Synthesis of TPM-BZ-Py POP from TPM-BZ-Br_4 and Py-T and their corresponding (b) FTIR spectra, (c) ^{13}C NMR spectra, and (d) DSC analyses.

strong hydrogen bond donor nature of Br enhances the electron density of nearby OH groups, which promotes the ability of the TPM-BZ-Br_4 monomer to open the oxazine ring. Therefore, the thermal polymerization was shifted from 254 °C to 236 °C and it absorbs less heat during thermal polymerization compared to the TPM-BZ monomer. Fig. 4(b) shows the FTIR spectra of the TPM-BZ-Br_4 at various temperatures. Similar to TPM-BZ, we also could observe two signals representing the oxazine ring at 944 and 1230 cm^{-1}. When the thermal polymerization temperature reached 270 °C for 2 h, the signal of the oxazine ring also disappeared, indicating ROP completely. The uncured TPM-BZ-Br_4 monomer's T_{d10} and char yield were 372 °C and 46 wt%, respectively, according to Fig. 4(c). The T_{d10} and char yield both rose to 389 °C and 50 wt%, respectively, after thermal ROP at 270 °C for 2 h. All of these results point to the development of a poly(TPM-BZ-Br_4) 3D network structure that is extensively cross-linked, as seen in Fig. 4(d). The activation energies (E_a) for TMP-BZ and TMP-BZ-Br_4 were determined to be 111.8 KJ/mol and 118.8 KJ/mol, respectively, using the Ozawa method. Additionally, when employing the Kissinger method, the activation energies for TMP-BZ and TMP-BZ-Br_4 were found to be 108.7 KJ/mol and 116.2 KJ/mol, respectively [Figure S7].

3.4. Synthesis, characterization, and thermal polymerization behavior of the 3D TPM-BZ-Py POP

Fig. 5(a) illustrates our synthesis steps for 3D TPM-BZ-Py POP through Sonogashira coupling from TPM-BZ-Br_4 and Py-T monomers. The reaction was carried out using $Pd(PPh_3)_4$ as a catalyst and DMF/Et_3N as a co-solvent for 3 days at 90 °C under a N_2 atmosphere. We also used FTIR, NMR, and DSC analyses to confirm the structure and investigate the polymerization of 3D TPM-BZ-Py POP. FTIR spectra as displayed in Fig. 5(b), allow us to identify the specific signals at 3280, 2198, and 1601 cm^{-1}, which correspond to the C≡C—H, C≡C, and C═C units, respectively, in the Py-T monomer. Similarly, the characteristic signals could be observed in TPM-BZ-Br_4 as mentioned above that corresponds to the C—O—C and the oxazine ring at 1230 and 944 cm^{-1}, respectively. After the Sonogashira coupling to from 3D TPM-BZ-Py POP, The emergence of new signals at 2190, 1230, and 935 cm^{-1} indicated the presence of C≡C stretching and the oxazine ring. Furthermore, the absorption at 3280 cm^{-1}, which is associated with the C—C—H unit of the Py-T monomer, was no longer observed, confirming the completing Sonogashira coupling to form 3D TPM-BZ-Py POP. As shown in NMR spectra (Fig. 5c), the ^{13}C NMR spectrum in solution displays signals for Py-T at 135.6–127.7, and 84.3 ppm, which correspond to the aromatic and C≡C carbons, respectively. The featured signals of TPM-BZ-Br_4 mentioned previously at 79.1, 61.9, and 48.4 ppm, representing the OCH_2N, a quaternary carbon atom, and $ArCH_2N$, respectively, were observed. Clearly, the solid-state ^{13}C NMR spectrum featured signals of 3D TPM-BZ-Py POP at 80.7, 62.9, and 48.7 ppm, representing the OCH_2N, a quaternary carbon atom, and $ArCH_2N$, respectively. In addition, the aromatic carbons were observed in the range of 156.2 to 111.3 ppm, indicating the successful synthesis of 3D TPM-BZ-Py POP. Finally, we could also observe that the thermal

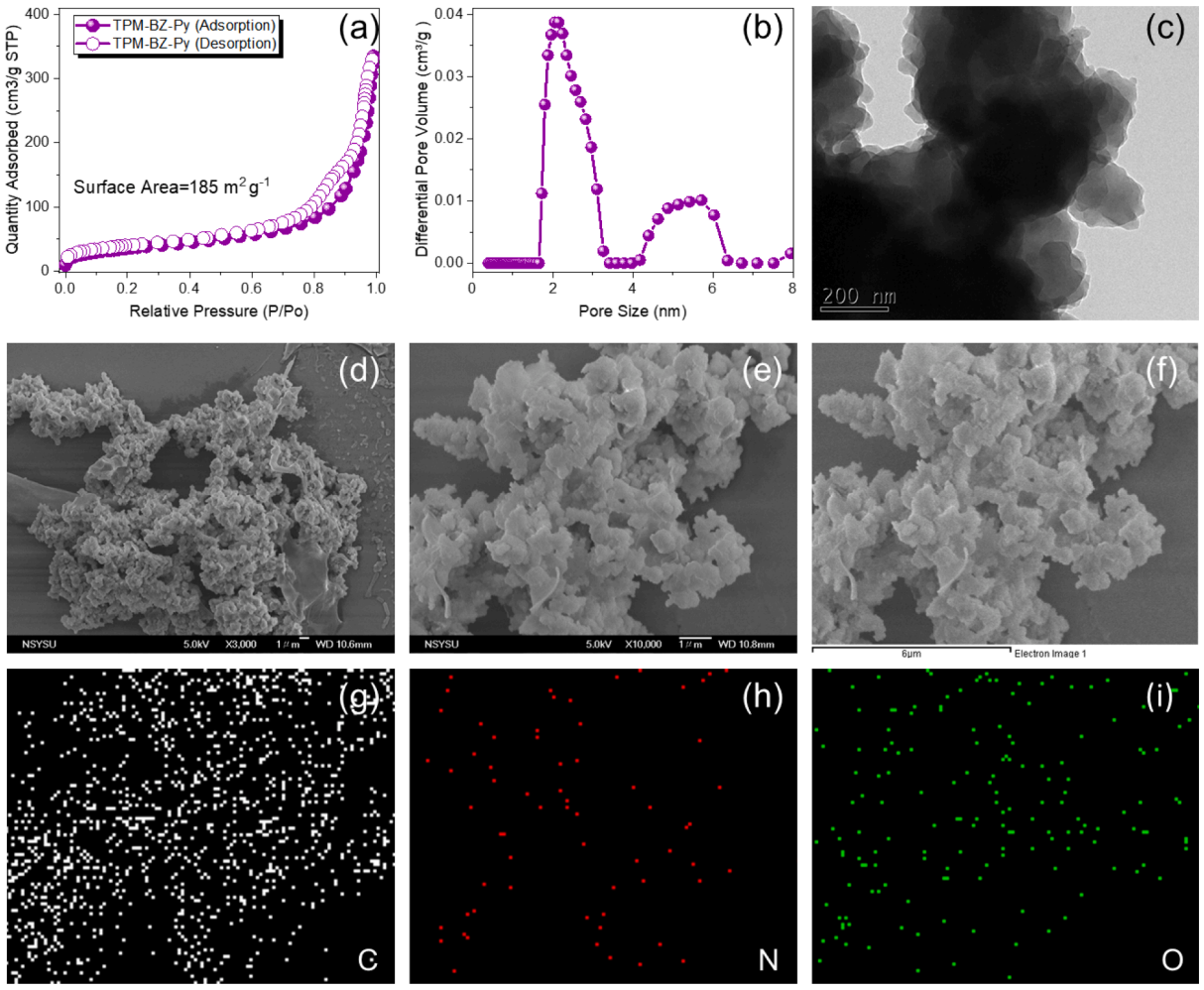

Fig. 6. (a) N_2 adsorption/desorption isotherms, (b) pore sizes, (c) TEM image, (d-f) SEM images and (g, h, i) EDS images including C, N, and O atoms of TPM-BZ-Py POP.

polymerization exothermic peaks from 236 °C significantly shifted to 303 °C, and the enthalpy from 90 J/g was significantly increased to 155 J/g. The utilization of Sonogashira coupling for the crosslinking structure-imposed limitations on the ROP of the oxazine ring. As a result, it became evident that the temperature of the exothermic peak for 3D TPM-BZ-Py POP was significantly higher compared to that of the TPM-BZ-Br_4 monomer. In addition, the higher enthalpy of 3D TPM-BZ-Py POP suggests an increased number of thermal active units, such as benzoxazine ring and triple bonds, after Sonogashira coupling. This effect may lead to a higher crosslinking density being achieved through ROP.

We measured N_2 adsorption/desorption isotherms at 77 K to determine the porosity of the 3D TPM-BZ-Py POP. Fig. 6(a) displays that the adsorption of N_2 by 3D TPM-BZ-Py POP is sharply increased at low relative pressure ($P/P_o < 0.1$), indicating a strong Van der Waals interaction between TPM-BZ-Py POP and N_2. According to the definition by IUPAC, the adsorption–desorption isotherm could be classified as a Type IV isotherm. Based on the Brunauer-Emmett-Teller (BET) analysis, the specific surface area of TPM-BZ-Py POP was measured to be 185 m^2 g^{-1} and the total pore volume was found to be 0.52 cm^3 g^{-1}. We used the non-local density functional theory (NLDFT) molecular dynamics method to determine that the average pore size distribution ranges from 1.65 to 3.41 nm (Fig. 6(b)), indicating a pore size falls between micropores and mesopores. Compared with previous BZ-linkage porous polymers such as THPT-BZ-TAPT POP with a specific surface area of ca. 72 m^2 g^{-1}, and CE-BZ-Py and CE-BZ-TPE POP with a specific surface area of 11.9 and 33.5 m^2 g^{-1}, respectively, the specific surface of TPM-BZ-Py POP is relatively higher. It is close to the fully BZ-linked TPA-BZ-DHTP POP (195 m^2 g^{-1}), but lower than some other 2D BZ-linked POPs [29,31,36,66,67]. This suggests that 3D TPM-BZ-Py POP exhibited a reasonable specific surface area considering its 3D structure, however, until now, such a phenomenon has not been previously reported. TEM and SEM images were used to observe the nanostructure of 3D TPM-BZ-Py POP. Fig. 6(c) shows a TEM image displaying the disordered nature of 3D TPM-BZ-Py POP and the existence of irregular microporous structures. Additionally, the surface morphologies were visualized through SEM images as shown in Fig. 6(d)-6(f), revealing the presence of irregular and interconnected spheres within the structure. The C, N, and O mapping based on SEM analyses (Fig. 6(g)-6(i) show the distribution and ratio of C, N, and O atoms in 3D TPM–BZ–Py POP.

Fig. 7(a) provides a schematic diagram illustrating the solid-state chemical transformation of poly(TPM-BZ-Py) POP following the thermal treatment of TPM-BZ-Py POP at 270 °C. After 3 h of thermal ROP at 270 °C, FTIR spectra (Fig. 7(b)) show the disappearance of signals representing the oxazine ring was disappeared at 935 and 1230 cm^{-1}. In addition, a broad peak in the range of 3700–2400 cm^{-1} indicates the existence of large quantities of OH groups leading to intermolecular and intramolecular hydrogen bonds [26,29,31,37]. The signal of the oxazine ring in the solid-state ^{13}C NMR spectrum (Fig. 7c) was also decreased at 80.7 ppm for OCH_2N units (overlapped with C≡C units) but totally disappeared at 48.7 ppm for $ArCH_2N$ units. We used TGA analysis as shown in Fig. 7(d) to investigate the T_{d10} and char yield for uncured TPM-BZ-Py POP, which were 377 °C and 41 wt%, respectively. After

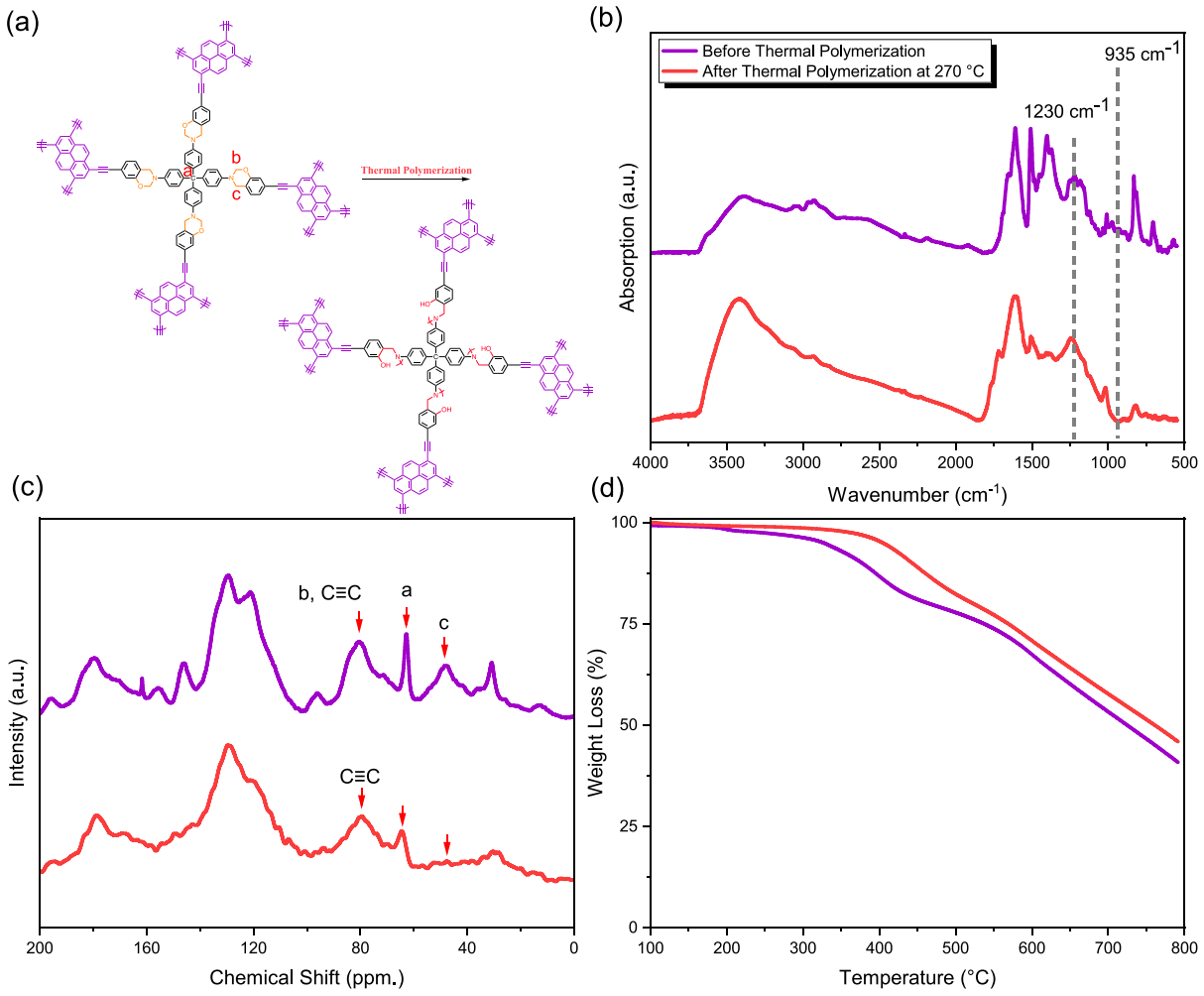

Fig. 7. (a) Schematic representation of the chemical structural change of the TPM-BZ-Py POP after thermal polymerization to form poly(TPM-BZ-Py) POP. (b – d) their corresponding (b) FTIR, (c) ^{13}C NMR and (d) TGA analyses.

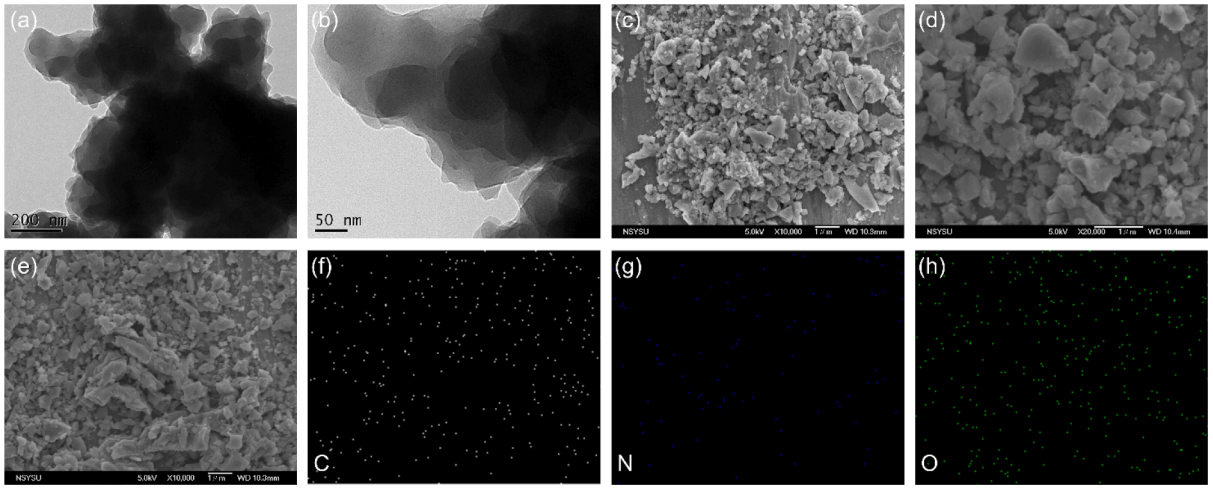

Fig. 8. (a, b) TEM images, (c, d, e) SEM images and (f, g, h) EDS images of C, N, O atoms of poly(TPM-BZ-Py) POP.

thermal ROP to form poly(TPM-BZ-Py) POP, which was significantly increased to 442 °C and 46 wt%, respectively. All results verified the formation of a highly 3D cross-linked structure of poly(TPM-BZ-Py) POP through solid-state chemical transformation.

Similarly, in the TEM images (Fig. 8(a-b)) and SEM images (Fig. 8(c-e)) after thermal ROP, we could find the presence of irregular and disordered structures. The surface of poly(TPM-BZ-Py) POP may contain a large number of phenolic OH groups and Mannich bridges. Further analyses of the SEM images using the C, N, and O mapping (Fig. 8(f)-(h)) express based on SEM analysis confirmed the distribution of C, N, and O

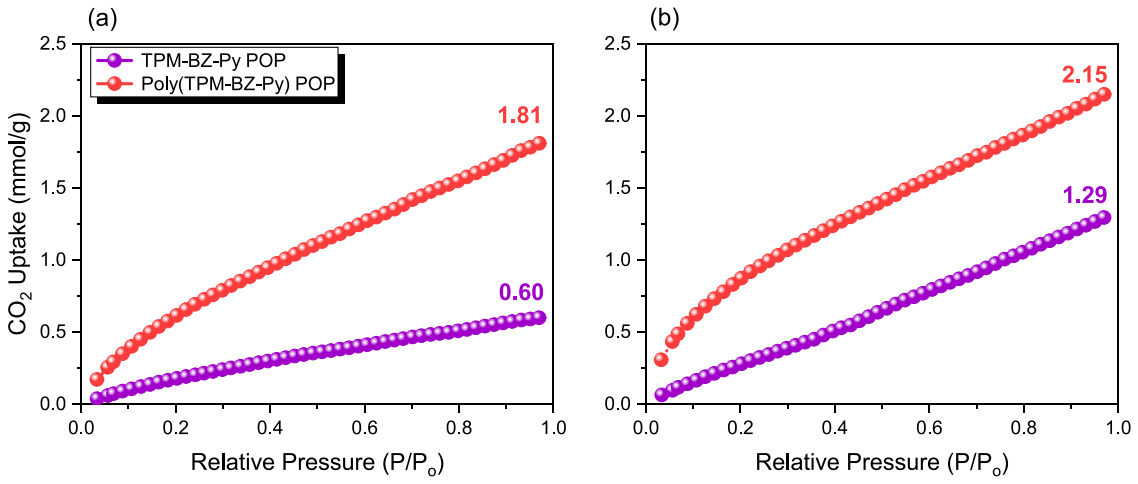

Fig. 9. (a) CO_2 uptake at 298 K and (b) at 273 K of TPM-BZ-Py POP and poly(TPM-BZ-Py) POP.

atoms throughout the poly(TPM-BZ-Py) POP, indicating their presence in dispersed form.

3.5. *CO_2 capture of the 3D TPM-BZ-Py POP*

The thermal ROP of TPM-BZ-Py POP in the solid state has been confirmed to undergo a one-step chemical transformation, resulting in the formation of phenolic OH and the Mannich bridge units. These newly formed functional units exhibit strong intermolecular interactions with guest components. One interesting application of this concept is in the field of CO_2 capture, where TPM-BZ-Py POP could serve as a model to investigate the changes during the solid-state chemical transformation after thermal ROP since this material possesses high porosity and excellent thermal stability. Since TPM-Py-BZ is a porous material, its high specific surface area could effectively capture gases. Therefore, we tested its ability to capture CO_2 through measured CO_2 capture experiments at 298 K (Fig. 9a) and 273 K (Fig. 9b) at 1 bar. The results displayed that CO_2 capture amounts of TPM-Py-BZ POP were 0.60 mmol g^{-1} (2.64 wt%) at 298 K and 1.29 mmol g^{-1} (7.96 wt%) at 273 K. After undergoing thermal ROP to form poly(TPM-Py-BZ) POP, it was significantly increased to 1.81 mmol g^{-1} (5.67 wt%) at 298 K and 2.15 mmol g^{-1} (9.46 wt%) at 273 K. The capability of the poly(TPM-Py-BZ) POP is higher than that of the TPM-Py-BZ POP because the former polymeric frameworks undergo a solid-state chemical transformation during the ROP, and a large number of phenolic OH groups and N atoms would appear, which could form strong hydrogen bonding through [OH···O═] and acid-base interactions [N···O═C] to increase CO_2 capability. The CO_2 capture capacity of our synthesized poly(TPM-Py-BZ) POP has a higher value (2.15 mmol g^{-1}) compared with other previously published structures [**Table S1**], such as Py-BSU CMP (1.45 mmol g^{-1}) [70], BOXPOP-1 (0.95 mmol g^{-1}) [66], BPOP-1 (0.98 mmol g^{-1}) [67], BPOP-2 (0.67 mmol g^{-1}) [67], COF-8 (1.43 mmol g^{-1}) [71], PTPA-3 (1.48 mmol g^{-1}) [72] and TPA-DHTP-BZ POP (0.97 mmol g^{-1}) [31] due to the existence of large amounts of N and phenolic OH units, which significantly enhance its CO_2 capture performance. Furthermore, we also determined the isosteric adsorption heats (Q_{st}) of the TPM-Py-BZ POP and poly(TPM-Py-BZ) POP based on their CO_2 adsorption results at 298 and 273 K according to the Clausius–Clapeyron equation. The Qst values of the TPM-Py-BZ POP and poly(TPM-Py-BZ) POP were 18.99 and 21.37 kJ/mol at a low adsorption of CO_2 (ca. 0.5 mmol/g), respectively. These results indicate that the poly(TPM-Py-BZ) POP could have more strong interaction with CO_2 molecules compared with TPM-Py-BZ POP, also suggesting the presence of significant N and phenolic OH units could enhance its CO_2 capture performance after thermal ROP.

4. Conclusions

To conclude, we have successfully synthesized a novel 3D benzoxazine-linked POP (TPM-BZ-Py) through a series of sequential steps involving Schiff base formation, $NaBH_4$ reduction, Mannich condensation, and Sonogashira-Hagihara coupling reactions. The structure characterization and the ROP behaviors were extensively investigated using various techniques including DSC, TGA, FTIR, and solid-state NMR analysis. By subjecting ROP via solid-state chemical transformation, the resulting TPM-BZ-Py POP exhibited exceptional thermal stability, characterized by a thermal decomposition temperature of 377 °C and a char yield of 41 wt%, which were notably enhanced to 442 °C and 46 wt%, respectively. Moreover, the TPM-BZ-Py POP displayed highly porous behavior, demonstrating a surface area of 185 m^2/g and a total pore volume of 0.52 cm^3/g. The obtained phenolic units and Mannich bridges after solid-state chemical transformation of poly(TPM-BZ-Py) POP exhibited better CO_2 capture ability due to the strong intermolecular H-bonding and acid/base interaction with CO_2 molecules. This work presents a new 3D BZ-linked POP featuring solid-state transformation ability, making it highly promising for applications in gas capture or separation.

CRediT authorship contribution statement

Mohamed Gamal Mohamed: Investigation, Methodology, Conceptualization, Supervision, Writing – original draft. **Chia-Chi Chen:** Methodology. **Kan Zhang:** Writing – original draft, Supervision. **Shiao-Wei Kuo:** Writing – original draft, Supervision.

Declaration of Competing Interest

The authors declare that they have no known competing financial interests or personal relationships that could have appeared to influence the work reported in this paper.

Data availability

The data that has been used is confidential.

Acknowledgments

This study was supported financially by the National Science and Technology Council, Taiwan, under contracts NSTC 112-2221-E-110-003 and 112-2223-E-110-002. The authors thank the staff at National Sun Yat-sen University for their assistance with the TEM (ID: EM022600) experiments. The authors also acknowledge the support

from the National Natural Science Foundation of China (No. 52073125).

Appendix A. Supplementary data

Supplementary data to this article can be found online at https://doi.org/10.1016/j.eurpolymj.2023.112551.

References

[1] C. Ru, T. Zhou, J. Zhang, X. Wu, P. Sun, P. Chen, L. Zhou, H. Zhao, J. Wu, X. Pan, Introducing Secondary Acceptors into Conjugated Polymers to Improve Photocatalytic Hydrogen Evolution, Macromolecules 54 (2021) 8839–8848, https://doi.org/10.1021/acs.macromol.1c00705.

[2] X. Shi, Z. Zhang, M. Wei, X. Wang, J. Wang, Y. Zhang, Y. Wang, Three-Dimensional Covalent Organic Framework Membranes: Synthesis by Oligomer Interfacial Ripening and Application in Precise Separations, Macromolecules 55 (2022) 3259–3266, https://doi.org/10.1021/acs.macromol.1c02333.

[3] Y. Ye, M.G. Mohamed, W.C. Chen, S.W. Kuo, Integrating the multiple functionalities in metalloporphyrin porous organic polymers enabling strong polysulfide anchoring and rapid electrochemical kinetics in Li–S batteries, J. Mater. Chem. A 11 (2023) 9112–9124, https://doi.org/10.1039/D2TA09232H.

[4] A. Abid, S. Razzaque, I. Hussain, B. Tan, Eco-Friendly Phosphorus and Nitrogen-Rich Inorganic-Organic Hybrid Hypercross-linked Porous Polymers via a Low-Cost Strategy, Macromolecules 54 (2021) 5848–5855, https://doi.org/10.1021/acs.macromol.1c00385.

[5] M.G. Mohamed, T.H. Mansoure, M.M. Samy, Y. Takashi, A.A.K. Mohammed, T. Ahamad, S.M. Alshehri, J. Kim, B.M. Matsagar, K.C.W. Wu, S.W. Kuo, Ultrastable Conjugated Microporous Polymers Containing Benzobisthiadiazole and Pyrene Building Blocks for Energy Storage Applications, Molecules 27 (2022) 2025, https://doi.org/10.3390/molecules27062025.

[6] M.G. Mohamed, W.C. Chang, S.V. Chaganti, S.U. Sharma, J.T. Lee, S.W. Kuo, Dispersions of ultrastable crown-ether functionalized triphenylamine and pyrene-linked porous organic conjugated polymers with single-walled carbon nanotube as the high-performance electrode for supercapacitor, Polym. Chem. 14 (2023) 4589–4601, https://doi.org/10.1039/D3PY00708A.

[7] M.G. Mohamed, A.M. Elewa, M.S. Li, S.W. Kuo, Construction and multifunctional of hypercrosslinked porous organic polymers containing ferrocene unit for high-performance iodine adsorption and supercapacitor, J. Taiwan Inst. Chem. Eng. 150 (2023), 105045, https://doi.org/10.1016/j.jtice.2023.105045.

[8] X. Guan, Y. Zhao, H. Pei, M. Zhao, Y. Wang, X. Zhou, M.G. Mohamed, S.W. Kuo, Y. Ye, Metalloporphyrin conjugated porous polymer in-situ grown on a Celgard separator as multifunctional polysulfide barrier and catalyst for high-performance Li-S batteries, Chem. Eng. J. 473 (2023), 144733, https://doi.org/10.1016/j.cej.2023.144733.

[9] T. Zhang, G. Xing, W. Chen, L. Chen, Porous organic polymers: a promising platform for efficient photocatalysis, Mater. Chem. Front. 4 (2020) 332–353, https://doi.org/10.1039/C9QM00633H.

[10] A.O. Mousa C.H. Chuang, S.W. M.G. Strategic Design and Synthesis of Ferrocene Linked Porous Organic Frameworks toward Tunable CO_2 Capture and Energy Storage. Int. J. Mol. Sci. 24 (2023) 12371. https://doi.org/10.3390/ijms241512371.

[11] A.O. Mousa, M.G. Mohamed, Z.I. Lin, C.H. Chuang, C.K. Chen, S.W. Kuo, Conjugated microporous polymers as a novel generation of drug carriers: A systemic study toward efficient carriers of tetracycline antibiotic, Eur. Polym. J. 196 (2023), 112254, https://doi.org/10.1016/j.eurpolymj.2023.112254.

[12] W.T. Chung, I.M.A. Mekhemer, M.G. Mohamed, A.M. Elewa, A.F.M. EL-Mahdy, H. H. Chou, S.W. Kuo, K.C.W. Wu, Recent advances in metal/covalent organic frameworks based materials: Their synthesis, structure design and potential applications for hydrogen production, Coord. Chem. Rev. 483 (2023), 215066, https://doi.org/10.1016/j.ccr.2023.215066.

[13] M.G. Mohamed, A.F.M. EL-Mahdy, M.G. Kotp, S.W. Kuo, Advances in porous organic polymers: syntheses, structures, and diverse applications, Mater. Adv. 3 (2022) 707–733, https://doi.org/10.1039/D1MA00771H.

[14] M.M. Samy, I.M.A. Mekhemer, M.G. Mohamed, M.H. Elsayed, K.H. Lin, Y.K. Chen, T.L. Wu, H.H. Chou, S.W. Kuo, Conjugated Microporous Polymers Incorporating Thiazolo[5,4-d]thiazole Moieties for Sunlight-Driven Hydrogen Production From Water, Chem. Eng. J. 446 (2022), 137158, https://doi.org/10.1016/j.cej.2022.137158.

[15] L. Sun, Y. Zou, Z. Liang, J. Yu, R. Xu, A one-pot synthetic strategy via tandem Suzuki-Heck reactions for the construction of luminescent microporous organic polymers, Polym. Chem. 5 (2014) 471–478, https://doi.org/10.1039/C3PY00980G.

[16] Y. Lan, C. Yang, Y. Zhang, W. An, H. Xue, S. Ding, P. Zhou, W. Wang, Pyrrolidine-based chiral porous polymers for heterogeneous organocatalysis in water, Polym. Chem. 10 (2019) 3298, https://doi.org/10.1039/C9PY00326F.

[17] M.G. Mohamed, E.C. Atayde Jr, B.M. Matsagar, J. Na, Y. Yamauchi, K.C.W. Wu, S. W. Kuo, Construction hierarchically mesoporous/microporous materials based on block copolymer and covalent organic framework, J. Taiwan Inst. Chem. Eng. 112 (2020) 180–192, https://doi.org/10.1016/j.jtice.2020.06.013.

[18] C. Liu, Y. Jin, Z. Yu, L. Gong, H. Wang, B. Yu, W. Zhang, J. Jiang, Transformation of Porous Organic Cages and Covalent Organic Frameworks with Efficient Iodine Vapor Capture Performance, J. Am. Chem. Soc. 144 (2022) 12390–12399, https://doi.org/10.1021/jacs.2c03959.

[19] M.G. Mohamed, M.M. Samy, T.H. Mansoure, S.U. Sharma, M.S. Tsai, J.H. Chen, J. T. Lee, S.W. Kuo, Dispersions of 1,3,4-Oxadiazole-Linked Conjugated Microporous Polymers with Carbon Nanotubes as a High-Performance Electrode for Supercapacitors, ACS Appl. Energy Mater. 5 (2022) 3677–3688, https://doi.org/10.1021/acsaem.2c00100.

[20] Y. Zhu, P. Xu, X. Zhang, D. Wu, Emerging Porous Organic Polymers for Biomedical Applications, Chem. Soc. Rev. 51 (2022) 1377–1414, https://doi.org/10.1039/D1CS00871D.

[21] X. Guan, F. Chen, Q. Fang, S. Qiu, Design and Applications of Three Dimensional Covalent Organic Frameworks, Chem. Soc. Rev. 49 (2022) 1357–1384, https://doi.org/10.1039/C9CS00911F.

[22] S.Y. Chang, A.M. Elewa, M.G. Mohamed, I.M.A. Mekhemer, M.M. Samy, K. Zhang, H.H. Chou, S.W. Kuo, Rational design and synthesis of bifunctional Dibenzo[g, p] chrysene-based conjugated microporous polymers for energy storage and visible light-driven photocatalytic hydrogen evolution Mater, Today Chem. 33 (2023), 101680, https://doi.org/10.1016/j.mtchem.2023.101680.

[23] M.G. Mohamed, C.C. Lee, A.F.M. EL-Mahdy, J. Lüder, M.H. Yu, Z. Li, Z. Zhu, C. C. Chueh, S.W. Kuo, Exploitation of two-dimensional conjugated covalent organic frameworks based on tetraphenylethylene with bicarbazole and pyrene units and applications in perovskite solar cells, J. Mater. Chem. A 8 (2020) 11448–11459, https://doi.org/10.1039/D0TA02956D.

[24] M.G. Mohamed, S.V. Chaganti, M.S. Li, M.M. Samy, S.U. Sharma, J.T. Lee, M. H. Elsayed, H.H. Chou, S.W. Kuo, Ultrastable Porous Organic Polymers Containing Thianthrene and Pyrene Units as Organic Electrode Materials for Supercapacitors, ACS Appl. Energy Mater. 5 (2022) 6442–6452, https://doi.org/10.1021/acsaem.2c00942.

[25] P.N. Singh, M.G. Mohamed, S.V. Chaganti, S.U. Sharma, M. Ejaz, J.T. Lee, S. W. Kuo, Rational Design of Ultrastable Conjugated Microporous Polymers Based on Pyrene and Perylene Units as High-Performance Organic Electrode Materials for Supercapacitor Applications, ACS Appl. Energy Mater. 16 (2023) 8277–8287, https://doi.org/10.1021/acsaem.3c01391.

[26] M.M. Samy, M.G. Mohamed, T.H. Mansoure, T.S. Meng, M.A.R. Khan, C.C. Liaw, S. W. Kuo, Solid state chemical transformations through ring-opening polymerization of ferrocene-based conjugated microporous polymers in host–guest complexes with benzoxazine-linked cyclodextrin, J. Taiwan Inst. Chem. Eng. 132 (2022), 104110, https://doi.org/10.1016/j.jtice.2021.10.010.

[27] M. Ejaz, M.M. Samy, Y. Ye, S.W. Kuo, M.G. Mohamed, Design Hybrid Porous Organic/Inorganic Polymers Containing Polyhedral Oligomeric Silsesquioxane/Pyrene/Anthracene Moieties as a High-Performance Electrode for Supercapacitor, Int. J. Mol. Sci. 24 (2023) 2501, https://doi.org/10.3390/ijms24032501.

[28] M.G. Mohamed, M.H. Elsayed, A.M. Elewa, A.F.M. El-Mahdy, C.H. Yang, A.A. K. Mohammed, H.H. Chou, S.W. Kuo, Pyrene-Containing Conjugated Organic Microporous Polymers for Photocatalytic Hydrogen Evolution from Water, Catal. Sci. Technol. 11 (2021) 2229–2241, https://doi.org/10.1039/D0CY02482A.

[29] M.G. Mohamed, T.C. Chen, S.W. Kuo, Solid-State Chemical Transformations to Enhance Gas Capture in Benzoxazine-Linked Conjugated Microporous Polymers, Macromolecules 54 (2021) 5866–5877, https://doi.org/10.1021/acs.macromol.1c00736.

[30] M.G. Mohamed, M.M. Samy, T.H. Mansoure, J.C. Li, W.C. Li, J.H. Chen, K. Zhang, S.W. Kuo, Microporous Carbon and Carbon/Metal Composite Materials Derived from Bio-Benzoxazine-Linked Precursor for CO_2 Capture and Energy Storage Applications, Int. J. Mol. Sci. 23 (2022) 347, https://doi.org/10.3390/ijms23010347.

[31] M. Ejaz, M.G. Mohamed, S.W. Kuo, Solid-state chemical transformation provides a fully benzoxazine-linked porous organic polymer displaying enhanced CO_2 capture and supercapacitor performance, Polym. Chem. 14 (2023) 2494–2509, https://doi.org/10.1039/D3PY00158J.

[32] M.M. Samy, M.G. Mohamed, S.U. Sharma, S.V. Chaganti, J.T. Lee, S.W. Kuo, An Ultrastable Tetrabenzonaphthalene-Linked conjugated microporous polymer functioning as a high-performance electrode for supercapacitors, J. Taiwan Inst. Chem. Eng. (2023), 104750, https://doi.org/10.1016/j.jtice.2023.104750.

[33] M.M. Samy, M.G. Mohamed, S.U. Sharma, S.V. Chaganti, T.H. Mansoure, J.T. Lee, T. Chen, S.W. Kuo, Constructing conjugated microporous polymers containing triphenylamine moieties for high-performance capacitive energy storage, Polymer 264 (2023), 125541, https://doi.org/10.1016/j.polymer.2022.125541.

[34] M.G. Mohamed, H.Y. Hu, M. Madhu, M.M. Samy, I.M.A. Mekhemer, W.L. Tseng, H. H. Chou, S.W. Kuo, Ultrastable two-dimensional fluorescent conjugated microporous polymers containing pyrene and fluorene units for metal ion sensing and energy storage, Eur. Polym. J. 189 (2023), 111980, https://doi.org/10.1016/j.eurpolymj.2023.111980.

[35] M.G. Mohamed, M.H. Elsayed, Y. Ye, M.M. Samy, A.E. Hassan, T.H. Mansoure, Z. Wen, H.H. Chou, K.H. Chen, S.W. Kuo, Construction of Porous Organic/Inorganic Hybrid Polymers Based on Polyhedral Oligomeric Silsesquioxane for Energy Storage and Hydrogen Production from Water, Polymers 15 (2023) 182, https://doi.org/10.3390/polym15010182.

[36] T.H. Weng, M.G. Mohamed, S.U. Sharma, S.V. Chaganti, M.M. Samy, J.T. Lee, S. W. Kuo, Ultrastable Three-Dimensional Triptycene- and Tetraphenylethene-Conjugated Microporous Polymers for Energy Storage, ACS Appl. Energy Mater. 5 (2022) 14239–14249, https://doi.org/10.1021/acsaem.2c02809.

[37] T.H. Weng, M.G. Mohamed, S.U. Sharma, I.M.A. Mekhemer, H.H. Chou, S.W. Kuo, Rationally Engineered Ultrastable Three-Dimensional (3D) Conjugated Microporous Polymers Containing Triptycene, Tetraphenylethene, and Benzothiadiazole Units as Exceptional High-Performance Organic Electrodes for Supercapacitors, ACS Appl. Energy Mater. 6 (2023) 9012–9024, https://doi.org/10.1021/acsaem.3c01933.

[38] M.G. Mohamed, M.M.M. Ahmed, W.T. Du, S.W. Kuo, Meso/Microporous Carbons from Conjugated Hyper-Crosslinked Polymers Based on Tetraphenylethene for High-Performance CO_2 Capture and Supercapacitor, Molecules 26 (2021) 738, https://doi.org/10.3390/molecules26030738.
[39] D. Stewart, D. Antypov, M.S. Dyer, M.J. Mitcher, A.P. Katsoulidis, P.A. Chater, F. Blanc, M.J. Rosseinsky, Stable and Ordered Amide Frameworks Synthesised under Reversible Conditions which Facilitate Error Checking, Nat. Commun. 8 (2017) 1102, https://doi.org/10.1038/s41467-017-01423-5.
[40] P.J. Waller, Y.S. Alfaraj, C.S. Diercks, N.N. Jarenwattananon, O.M. Yaghi, Conversion of Imine to Oxazole and Thiazole Linkages in Covalent Organic Frameworks, J. Am. Chem. Soc. 140 (2018) 9099–9103, https://doi.org/10.1021/jacs.8b05830.
[41] H. Liu, J. Chu, Z. Yin, X. Cai, L. Zhuang, H. Deng, Covalent Organic Frameworks Linked by Amine Bonding for Concerted Electrochemical Reduction of CO_2, Chem. 4 (2018) 1696–1709, https://doi.org/10.1016/j.chempr.2018.05.003.
[42] F. Haase, E. Troschke, G. Savasci, T. Banerjee, V. Duppel, S. Dorfler, M.M. J. Grundei, A.M. Burow, C. Ochsenfeld, S. Kaskel, B.V. Lotsch, Topochemical Conversion of an Imine- into A Thiazole-Linked Covalent Organic Framework Enabling Real Structure Analysis, Nat. Commun. 9 (2018) 2600, https://doi.org/10.1038/s41467-018-04979-y.
[43] P.J. Waller, S.J. Lyle, T.O. Popp, C.S. Diercks, J.A. Reimer, O.M. Yaghi, Chemical Conversion of Linkages in Covalent Organic Frameworks, J. Am. Chem. Soc. 138 (2016) 15519–15522, https://doi.org/10.1021/jacs.6b08377.
[44] C. Zhao, H. Lyu, Z. Ji, C. Zhu, O.M. Yaghi, Ester-Linked Crystalline Covalent Organic Frameworks, J. Am. Chem. Soc. 142 (2020) 14450–14454, https://doi.org/10.1021/jacs.0c07015.
[45] S.J. Lyle, T.O.S. Popp, P.J. Waller, X. Pei, J.A. Reimer, O.M. Yaghi, Multistep Solid-State Organic Synthesis of Carbamate-Linked Covalent Organic Frameworks, J. Am. Chem. Soc. 141 (2019) 11253–11258, https://doi.org/10.1021/jacs.9b04731.
[46] Q. Ma, X. Liu, H. Wang, Q. Zhuang, J. Qian, Construction of novel benzoxazine-linked covalent organic framework with antimicrobial activity via postsynthetic cyclization, Mater. Today Chem. 23 (2022), 100707, https://doi.org/10.1016/j.mtchem.2021.100707.
[47] M.G. Mohamed, S.W. Kuo, Crown Ether-Functionalized Polybenzoxazine for Metal Ion Adsorption, Macromolecules 53 (2020) 2420–2429, https://doi.org/10.1021/acs.macromol.9b02519.
[48] X. Shen, L. Cao, Y. Liu, J. Dai, X. Liu, J. Zhu, S. Du, How Does the Hydrogen Bonding Interaction Influence the Properties of Polybenzoxazine? An Experimental Study Combined with Computer Simulation, Macromolecules 51 (2018) 4782–4799, https://doi.org/10.1021/acs.macromol.8b00741.
[49] B. Lochab, M. Monisha, N. Amarnath, P. Sharma, S. Mukherjee, H. Ishida, Review on the Accelerated and Low-Temperature Polymerization of Benzoxazine Resins: Addition Polymerizable Sustainable Polymers, Polymers 13 (2021) 1260, https://doi.org/10.3390/polym13081260.
[50] S. Zhang, Q. Ran, Q. Fu, Y. Gu, Thermal responsiveness of hydrogen bonding and dielectric property of polybenzoxazines with different Mannich bridge structures, Polymer 175 (2019) 302–309, https://doi.org/10.1016/j.polymer.2019.05.058.
[51] Y. Lyu, H. Ishida, Natural-Sourced Benzoxazine Resins, Homopolymers, Blends and Composites: A Review of Their Synthesis, Manufacturing and Applications. Prog. Polym. Sci. 99 (2019), 101168, https://doi.org/10.1016/j.progpolymsci.2019.101168.
[52] M.G. Mohamed, S.W. Kuo, Functional Silica and Carbon Nanocomposites Based on Polybenzoxazines, Macromol. Chem. Phys. 220 (2019) 1800306, https://doi.org/10.1002/macp.201800306.
[53] M.G. Mohamed, C.J. Li, C.M.A.R. Khan, C.C. Liaw, K. Zhang, S.W. Kuo, Formaldehyde-Free Synthesis of Fully Bio-Based Multifunctional Bisbenzoxazine Resins from Natural Renewable Starting Materials, Macromolecules 55 (2022) 3106–3115, https://doi.org/10.1021/acs.macromol.2c00417.
[54] C.Y. Chen, W.C. Chen, M.G. Mohamed, Z.Y. Chen, S.W. Kuo, Highly Thermally Stable, Reversible, and Flexible Main Chain Type Benzoxazine Hybrid Incorporating Both Polydimethylsiloxane and Double-Decker Shaped Polyhedral Silsesquioxane Units through Diels-Alder Reaction, Macromol. Rapid Commun. 44 (2023) 2200910, https://doi.org/10.1002/marc.202200910.
[55] R. Yang, N. Li, C.J. Evans, S. Yang, K. Zhang, Phosphaphenanthrene-Functionalized Benzoxazines Bearing Intramolecularly Hydrogen-Bonded Phenolic Hydroxyl: Synthesis, Structural Characterization, Polymerization Mechanism, and Property Investigation, Macromolecules 56 (2023) 1311–1323, https://doi.org/10.1021/acs.macromol.3c00028.
[56] X.L. Sha, P. Fei, B. Shen, J. Chen, Z. Liu, Y. Sun, J.T. Miao, Solvent-free Synthesis of Alkynyl-Based Biobased Benzoxazine Resins with Excellent Heat Resistance, ACS Appl. Polym. Mater. 5 (2023) 3015–3022, https://doi.org/10.1021/acsapm.3c00183.
[57] H. Puozzo, S. Saiev, L. Bonnaud, J.D. Winter, R. Lazzaroni, D. Beljonne, Robust and Direct Route for the Development of Elastomeric Benzoxazine Resins by Copolymerization with Amines, Macromolecules 55 (2022) 10831–10841, https://doi.org/10.1021/acs.macromol.2c01593.
[58] Y. Kobzar, K.Y. Fatyeyeva, A Simple Solvent-Free Strategy of Polybenzoxazine Film Elaboration with Controllable Performance via Molecular Weight Regulation between Cross-Linking Knots, Macromolecules 55 (2022) 9384–9396, https://doi.org/10.1021/acs.macromol.2c00781.
[59] X. Zhang, M.G. Mohamed, Z. Xin, S.W. Kuo, A tetraphenylethylene-functionalized benzoxazine and copper(II) acetylacetonate form a high-performance polybenzoxazine, Polymer 201 (2020), 122552, https://doi.org/10.1016/j.polymer.2020.122552.
[60] M.M. Samy, M.G. Mohamed, S.W. Kuo, Pyrene-functionalized tetraphenylethylene polybenzoxazine for dispersing single-walled carbon nanotubes and energy storage, Compos. Sci. Technol. 199 (2020), 108360, https://doi.org/10.1016/j.compscitech.2020.108360.
[61] S. Mukherjee, N. Amarnath, B. Lochab, Oxazine Ring-Substituted 4th Generation Benzoxazine Monomers & Polymers: Stereoelectronic Effect of Phenyl Substituents on Thermal Properties, Macromolecules 54 (2021) 10001–10016, https://doi.org/10.1021/acs.macromol.1c01582.
[62] Z. Deliballi, B. Kiskan, Y. Yagci, Advanced Polymers from Simple Benzoxazines and Phenols by Ring-Opening Addition Reactions, Macromolecules 53 (2020) 2354–2361, https://doi.org/10.1021/acs.macromol.0c00225.
[63] K. Zhang, Y. Liu, H. Ishida, Polymerization of an AB-Type Benzoxazine Monomer toward Different Polybenzoxazine Networks: When Diels-Alder Reaction Meets Benzoxazine Chemistry in a Single-Component Resin, Macromolecules 52 (2019) 7386–7395, https://doi.org/10.1021/acs.macromol.9b01581.
[64] J.Y. Wu, M.G. Mohamed, S.W. Kuo, Directly synthesized nitrogen-doped microporous carbons from polybenzoxazine resins for carbon dioxide capture, Polym. Chem. 8 (2017) 5481–5489, https://doi.org/10.1039/C7PY01026E.
[65] H.R. Abuzeid, A.F.M. El-Mahdy, M.M.M. Ahmed, S.W. Kuo, Triazine-Functionalized Covalent Benzoxazine Framework for Direct Synthesis of N-Doped Microporous Carbon, Polym. Chem. 10 (2019) 6010–6020, https://doi.org/10.1039/C9PY01231A.
[66] S. Xu, J. He, S. Jin, B. Tan, Heteroatom-Rich Porous Organic Polymers Constructed by Benzoxazine Linkage with High Carbon Dioxide Adsorption Affinity, J. Colloid Interface Sci. 509 (2018) 457–462, https://doi.org/10.1016/j.jcis.2017.09.009.
[67] X. Sun, J. Li, W. Wang, Q. Ma, Constructing Benzoxazine-Containing Porous Organic Polymers for Carbon Dioxide and Hydrogen Sorption, Eur. Polym. J. 107 (2018) 89–95, https://doi.org/10.1016/j.eurpolymj.2018.07.043.
[68] Y. Xie, J. Li, C. Lin, B. Gui, C. Ji, D. Yuan, J. Sun, C.J. Wang, Three-Dimensional Large-Pore Covalent Organic Framework with stp Topology, J. Am. Chem. Soc. 143 (2021) 7279–7284, https://doi.org/10.1021/jacs.1c03042.
[69] S. Shukla, A. Mahata, B. Pathak, B. Lochab, Cardanol benzoxazines – interplay of oxazine functionality (mono to tetra) and properties, RSC Adv. 5 (2015) 78071–78080, https://doi.org/10.1039/C5RA14214H.
[70] M.G. Mohamed, S.Y. Chang, M. Ejaz, M.M. Samy, A.O. Mousa, S.W. Kuo, Design and Synthesis of Bisulfone-Linked Two-Dimensional Conjugated Microporous Polymers for CO2 Adsorption and Energy Storage, Molecules 28 (2023) 3234, https://doi.org/10.3390/molecules28073234.
[71] H. Furukawa, O.M. Yaghi, Storage of Hydrogen, Methane, and Carbon Dioxide in Highly Porous Covalent Organic Frameworks for Clean Energy Applications, J. Am. Chem. Soc. 131 (2009) 8875–8883, https://doi.org/10.1021/ja9015765.
[72] Y. Liao, J. Weber, C.F.J. Faul, Conjugated microporous polytriphenylamine networks, Chem. Commun. 50 (2014) 8002–8005, https://doi.org/10.1039/C4CC03026.